

Classification: Physical Science, applied physics

Multiconfigurational Nature of 5f Orbitals in Uranium and Plutonium Intermetallics

C. H. Booth¹, Yu Jiang¹, D. L. Wang², J. N. Mitchell³, P. H. Tobash³, E. D. Bauer⁴, M. A. Wall⁵, P. G. Allen⁵, D. Sokaras⁶, D. Nordlund⁶, T.-C. Weng⁶, M. A. Torrez⁴, and J. L. Sarrao⁷

¹Chemical Sciences Division, Lawrence Berkeley National Laboratory, Berkeley, California 94720, USA

²Nuclear Sciences Division, Lawrence Berkeley National Laboratory, Berkeley, California 94720, USA

³Materials Science and Technology Division, Los Alamos National Laboratory, Los Alamos, New Mexico 87545, USA

⁴Materials Physics and Applications Division, Los Alamos National Laboratory, Los Alamos, New Mexico 87545, USA

⁵Condensed Matter and Materials Division, Livermore National Laboratory, Livermore, California 94550, USA

⁶Stanford Synchrotron Radiation Lightsource, SLAC National Accelerator Laboratory, Menlo Park, CA 94025, USA

⁷Science Program Office- Office of Science, Los Alamos National Laboratory, Los Alamos, New Mexico 87545, USA

Corresponding author:

Corwin H. Booth

Chemical Science Division

MS 70A-1150

Berkeley, CA 94720 USA

Voice: 510-486-6079

FAX: 510-486-5596

Email: chbooth@lbl.gov

Web: <http://lise.lbl.gov/chbooth>

Author Contributions. E.D.B., J.N.M., P.T., M.A.T., J.L.S., and M.A.W. prepared the samples and performed basic characterization. Y.J., C.H.B., D.L.W., and E.D.B. performed the X-ray experiments. T.-C.W., D.S., and D.N. prepared the beamline and also participated in the measurements and interpretation. C.H.B. and Y.J. analyzed the X-ray data. C.H.B., P.G.A., and E.D.B. conceptualized the project. C.H.B. wrote the paper with input from all authors and supervised the project. All authors discussed the results and commented on the manuscript.

Abstract:

Uranium and plutonium's 5f electrons are tenuously poised between strongly bonding with ligand spd-states and residing close to the nucleus. The unusual properties of these elements and their compounds (eg. the six different allotropes of elemental plutonium) are widely believed to depend on the related attributes of f-orbital occupancy and delocalization, for which a quantitative measure is lacking. By employing resonant x-ray emission spectroscopy (RXES) and x-ray absorption near-edge structure (XANES) spectroscopy and making comparisons to specific heat measurements, we demonstrate the presence of multiconfigurational f-orbital states in the actinide elements U and Pu, and in a wide range of uranium and plutonium intermetallic compounds. These results provide a robust experimental basis for a new framework for understanding the strongly-correlated behavior of actinide materials.

\body

The magnetic and electronic properties of actinide (An) materials have long defied understanding, where scientists prior to World War II (and even Mendeleev) placed the actinide series underneath the 5d transition series in the periodic table. The reason for such confusion is that the 5f orbital is intermediate between localized, as generally are the 4f orbitals in the lanthanide series, and delocalized, such as occurs in the d-orbitals of the transition metals. In those two limiting cases, well defined methodologies exist that account for their magnetic behavior, such as Hund's Rules, crystal-field theory, and quenched angular momentum theory. No similarly successful theory exists for the intermediate localization that occurs in elemental U, Np, and Pu, and their intermetallic compounds, and yet the consequences are likely fundamental toward understanding their complex behavior (1, 2).

Although the degree of f-electron localization is widely recognized as the dominant factor in determining the structural, magnetic, and electronic properties of the actinides, for instance, in determining basic crystal bonding (3), experimental methods for determining the f-orbital occupancy have generally failed to yield quantitative measurements, although some exceptions exist. For example, elemental Pu is thought to have an f-orbital occupancy near 5, close to that expected for a $5f^5$ ground-state configuration (Pu^{3+}), based on photoemission, $N_{4,5}$ -edge x-ray absorption, and electron-energy loss spectroscopy (4, 5). In addition to these examples, several researchers have shown that so-called "two-fluid", or "dual nature", models of the 5f orbitals, whereby some fraction of the f-electrons contribute to delocalized behavior and the rest contribute to the more localized, local moment behavior, can successfully describe some properties (6), such as coexistent antiferromagnetism and superconductivity in CeRhIn_5 (7), the inelastic neutron scattering of UPd_2Al_3 (8), de Haas-van Alphen frequencies of UPt_3 (9), and the photoemission spectra of PuCoGa_5 and PuIn_3 (10). Such mixed behavior also manifests itself in the spin and orbital components of the angular momentum (11)—important quantities for understanding the absence of magnetism in plutonium (12). These results rely on fractional f-occupancies, especially in the delocalized channel. Recent Dynamical

Mean-Field Theory (DMFT) calculations by Shim, Haule, and Kotliar (13) suggest that, while the average f -occupancy is an important quantity, the actual ground state in elemental plutonium may require a more complete description. In particular, they find that, unlike cerium and ytterbium intermetallics which are described as dominated by two valence configurations (f^0 and f^1 for Ce^{4+} and Ce^{3+} , f^{13} and f^{14} for Yb^{3+} and Yb^{2+}), a description of elemental plutonium actually requires three valence configurations, f^4 , f^5 , and f^6 . Here, we present both x-ray absorption near-edge structure (XANES) and resonant x-ray emission spectroscopy (RXES) data collected at the actinide L_3 edge in a wide variety of uranium and plutonium intermetallics that not only points to the necessity of a multiconfigurational ground state for understanding of elemental plutonium, but also demonstrates the wide applicability of such multiconfigurational ground states in actinide intermetallics in general.

There are some advantages to using L_3 -edge spectroscopy for obtaining f -occupancies, especially for multiconfigurational states. At this X-ray absorption edge, a $2p_{3/2}$ core electron is excited into, primarily, a state of d symmetry, where the number of unoccupied $6d$ states is only a weak function of the f -occupancy (Fig. 1a). If a multiconfigurational f -state exists, its otherwise-degenerate components are split by the core-hole interaction, as the different number of f -electrons in each configuration screen the core hole differently. Since the total number of unoccupied d -states is approximately fixed, the excitation amplitude into any split states is proportional to that particular configuration's electronic occupancy. By associating a given peak with a particular configuration, the relative weight to each configuration can be simply determined. For instance, in RXES results on Yb intermetallics (14, 15), the integrated intensity I_{13} and I_{14} of features identified as due to the f^{13} and f^{14} configurations give the f -hole occupancy $n_f = I_{13}/(I_{13}+I_{14})$. Similar methods have long been applied in XANES spectroscopy (16). While these measurements give the f -occupancy and configuration fractions in the excited state, which includes the core-hole and the outgoing photoelectron, such final-state occupancies are within several percent of those obtained using more sophisticated treatments for deep core-level excitations (17).

In this study, the An L_3 -edge XANES data collected from α -U, α -Pu, and δ -Pu(1.9 at% Ga) along with 17 other uranium and 9 plutonium intermetallic samples delineate the correspondence between the edge position and localization of the $5f$ electrons. Pu L_3 -edge XANES data are shown for typical Pu materials from this study in Fig. 1b. Similar U data are in Supporting Information (SI). The position of the main peak, known as the "white line" position, is shown in Fig. 1c and 1d as a function of the shift from the white-line position of the α -phase of the actinide (i.e. α -U or α -Pu), ΔE_α . Large shifts in ΔE_α are observed, as are broadened white-line features for some compounds. Individual peaks are not observed, and so obtaining state configuration fractions is not possible from these data. The Sommerfeld coefficient to the linear component of the low-temperature specific heat, γ , is used as a measure of the degree of localization. The value of γ often is the defining quantity for heavy-fermion behavior, since it is proportional the effective carrier mass; that is, it is proportional to the density of states, ρ , at the Fermi level. In this sense, the flatter bands have a large linear specific heat, and are considered to have more localized character due to a higher f -orbital occupancy (18). This higher occupancy could

be due to f-orbital hybridization with the conduction band, as in a Kondo model, or due to direct involvement of the f-band at the Fermi level, which is uncommon in the lanthanides. In the case of samples with magnetic transitions (many of the more localized materials are antiferromagnetic in their ground state), γ is determined at temperatures above any transitions to remove the effect of changes in magnetic degrees of freedom (19). Some of these transition temperatures are as high as 30 K, and so large errors are reported due to the larger contribution of phonon vibrations to the specific heat at such temperatures. (More information regarding the specific heat, including all the values of γ and transition temperatures, is available in SI.) As shown in Figs. 1c and 1d, there is a strong correlation between ΔE_α and the degree of localization of the 5f electrons, as measured by γ . This correspondence is explained by considering that the higher f-occupancy (i.e., larger γ) implies more localized f-electrons are available for screening the 2p_{3/2} core hole, generating a more negative ΔE_α , as observed.

These XANES results indicate that the final-state shifts of the white line correlate well with a ground-state measurement of the density of states. While individual peaks are not observed in the white lines (Fig. 1b), there appears to be a correspondence between the width of the white line and the overall energy shift, consistent with two or more configurations, although possibly also indicating a broader 6d band.. Focusing on the U intermetallics, $\Delta E_\alpha > 6.5$ eV between the end-point samples, UCd₁₁ and α -U. Using energy shifts between known oxidation states, for instance, between U³⁺ and U⁴⁺ oxides, a change of one electron corresponds to about 4 eV. A similar value is found between Pu oxides (20). A 6.5 eV shift implies a change in f-occupancy of nearly 1.5 electrons. While this is possible, we point out that a ~ 1.5 eV shift is observed between UPd₃, which has an f² configuration and is one of the few An intermetallic materials measured with a relatively well-known f-occupancy (21), and UO₂, which is also f². We contend that such a shift is due to greater screening of the core-hole in UPd₃ due to conduction electrons (22). Such conduction electron screening reduces the Coulombic attraction between the core hole and the photoelectron, and may also affect excitations into the lower unoccupied d-states just above the Fermi level. Although this effect will be roughly constant between metals, it makes determining f-occupancy from the measured edge shifts less reliable.

To gain quantitative information about the valence in elemental U and Pu and their compounds, U and Pu L₃-edge RXES data (23-26) were collected at the An L _{α 1} emission line (3d_{5/2}→2p_{3/2} corresponding to an emission energy E_E of about 14.2 keV for Pu and 13.6 keV for U, see final state in Fig. 1a). Fig. 2 shows the X-ray emission spectra (XES) and the RXES for UCd₁₁ and α -Pu at several incident energies E_I as a function of the transfer energy, $E_T = E_I - E_E$. Data on PuSb₂, UCoGa₅, and δ -Pu are available in the SI. Since excitations into the continuum imply that states are always available above a threshold energy and E_E has a constant distribution for these states, $E_T \propto E_I$ for fluorescence lines. Excitations into unoccupied states with discrete energy levels, on the other hand, have a distribution with a constant E_T as a function of E_I . The upper panels are well below the fluorescence threshold, and show excitations that are at approximately fixed E_T as E_I is increased in the lower panels, although the amplitude of the three individual features varies with E_I . It is important to note that excitations into states below

the fluorescence threshold are not, in fact, discrete (although that is how they are referred to below) in these materials, but have a finite bandwidth, and so E_T is expected to vary as much as a few eV. The bottom panels (Figs. 2*b* and 2*d*) show the fluorescence line as a dominant feature with a E_T that will increase linearly as E_I increases further.

These RXES data clearly show changes in lineshape due to multiple excitation features as a function of incident energy—made possible by the improved resolution of this technique (27), which is set by the $3d_{5/2}$ orbital (about 4 eV) rather than the $2p_{3/2}$ (between 7 and 10 eV), and the ability to separate excitations into the continuum. To determine the individual contributions to that lineshape, we follow standard procedures set forth by Dallera et al. (14, 15), and find a Lorentzian lineshape for both the fluorescence and the discrete excitation contributions. In general, three excitations are required to fit most of the data. Although E_T varies by 1 or 2 eV with E_I for the lowest- E_T excitation (the f^3 U L_3 and the f^6 for Pu L_3), these three excitations remain well separated by about 4 eV in E_T , consistent with a difference of one electron occupancy for each state. The relative weights of each configuration and the fluorescence peak are shown in Fig. 3 as a function of E_I . The total configuration fractions are then obtained by integrating these results over E_I (Table 1). Absolute errors are estimated by altering the lineshape for the standard discrete excitation, and are about 10% (one such alteration is discussed in the SI). Relative errors between these measurements are about 2%. (Unfortunately, the PuSb₂ data do not allow for such a determination, since the bandwidth-related shifts in E_T are too large, see SI). While these below-threshold excitations allow for a measurement of the state configuration fractions and the overall f -occupancy, the RXES data also allow for the determination of the fluorescence threshold energy shifts. These shifts (Fig. 3*c* and 3*f*) indicate differences in the total screening of the core hole and include the effect of differences in the conduction electron density.

These results have important implications for understanding the nature of the ground states for all the measured actinide materials in Fig. 1. In particular, Pu in the α - and δ -forms is best described with partially delocalized and strongly multiconfigurational f -orbitals, both in observed changes in the XANES and the broad features in the RXES, each as compared to data from more localized samples such as UCd₁₁ and PuSb₂. Indeed, qualitative agreement is obtained with DMFT calculations (13) for the configuration f^4 , f^5 , and f^6 fractions in δ -Pu, which indicate about 60% f^5 configuration, compared to about (38±10)% measured here (see Table caption for discussion of error estimates). In addition, DMFT predicts a difference in the total f -occupation $\Delta n_f=0.2$ between α - and δ -Pu, whereas the RXES results give $\Delta n_f=0.12\pm 0.02$ (Table 1). Furthermore, within the estimated absolute errors, a multiconfigurational ground state occurs even for our most localized actinide sample, i.e., UCd₁₁, raising the fundamental question of whether any true U³⁺ intermetallic compound actually exists. Our results not only provide an accurate measure of the f -occupancy in plutonium for the first time, they advance a new paradigm for understanding the light actinides based upon a 5 f -electron multiconfigurational ground state that goes far beyond a “dual nature” scenario.

Materials and Methods

Sample preparation. Metallic δ - and α -phase samples were first melted and then high temperature annealed to remove any lattice defects and He gas that accumulated while aging at room temperature. Subsequently, 2.3 mm diameter discs were punch pressed, lapped, and polished, using a succession of finer grit lapping films ending in a 1 μm surface finish and a final thickness of 70 μm . The samples were then dip-coated with liquid Kapton and cured at 150 $^{\circ}\text{C}$ for 2 hours. This encasement greatly reduces the oxidation of the metallic Pu over time. The final curing at 150 $^{\circ}\text{C}$ also reverts any potential damage or phase due to the mechanical polishing process. All sample preparation/processing was done in an inert atmosphere glovebox for safety and for the minimizing of the continuous oxidative nature of these materials.

Single crystals of all Pu intermetallic compounds were grown by the molten metal flux growth technique (28), as were single crystals of UCoGa_5 , $\text{UM}_2\text{Zn}_{20}$ ($M=\text{Fe, Co, Ru}$), USn_3 , UCd_{11} , and U_2Zn_{17} . Polycrystalline samples of UAuCu_4 , UAu_3Ni_2 , UCu_5 , UPt_3 , UNi_2Al_3 , URu_2Si_2 , UPd_2Al_3 , and UPd_3 were synthesized by arc-melting the elements on a water-cooled Cu hearth with a Zr getter under an ultra-high pressure (UHP) Ar atmosphere. In some cases, the arc-melted samples were annealed under vacuum to improve crystallinity.

XANES. Nearly all of the X-ray data were collected in fluorescence mode on single solid pieces of material. Exceptions are XANES data from PuCoGa_5 , PuGa_3 , and PuAl_2 . Each of these samples was ground with a mortar and pestle and passed through a 30 μm sieve. The resulting powder was mixed with boron nitride or, in the case of PuAl_2 only, brushed onto clear adhesive tape. XANES data from these powder samples were collected in transmission mode. The samples were loaded into a LHe-flow cryostat and data were collected with the samples near 30 K, although no changes with temperature have been observed up to room temperature. All fluorescence data in Fig. 1 were measured on BL 10-2 or 11-2 at the Stanford Synchrotron Radiation Lightsource (SSRL) over a period of 10 years, both before and after the upgrade to that facility that took place in 2003. All data were collected using a double-crystal $\text{Si}(220)$ monochromator, half-tuned to remove unwanted harmonic energies from the X-ray beam. The fluorescence data were collected using a multi-element solid-state Ge detector and were corrected for dead time, and were also corrected for self-absorption using the program FLUO (29). All monochromator energies were calibrated to the first inflection point of the L_3 edge absorption from either UO_2 at 17166.0 eV (30) or PuO_2 at 18062.3 eV (20).

RXES. RXES data were collected at room temperature using the a 7-crystal Johann-type x-ray emission spectrometer (25) at the wiggler beamline 6-2 that incorporates a LN_2 cooled double-crystal $\text{Si}(311)$ monochromator, and Rh-coated collimating and focusing mirrors. U $L_{\alpha 1}$ (13.6 keV) emission was measured using $\text{Ge}(777)$ analyzer crystals, and Pu $L_{\alpha 1}$ (14.2 keV) emission was measured using $\text{Si}(777)$ analyzer crystals. The analyzer energy was calibrated using the nearby elastic peak from the 999 reflection and the already-calibrated monochromator energy. The resolution was measured from the elastically scattered beam to be 1.4 eV and 1.7 eV, respectively, at the An $L_{\alpha 1}$ emission energies.

Determination of the lineshapes follows the methods of Dallera et al. (14). The intrinsic lifetime broadening (27) of any observed features is set by the $3d_{5/2}$ orbital (about 4 eV), rather than the $2p_{3/2}$ (between 7 and 10 eV). The fluorescence peak lineshape and position were determined at an E_I that was well above threshold. The U L_3 edge data were fit using $E_{L\alpha 1} = 13616.1$ eV (UCd₁₁) or 13617.1 eV (UCoGa₅), and a width $\Gamma_F = 5.9$ eV. The Pu L_3 edge data were fit using $E_{L\alpha 1} = 1477.7$ eV and a width $\Gamma_F = 6.5$ eV. The normalized emission lineshape from the discrete excitations was obtained well below threshold for the most localized samples measured, namely UCd₁₁ and PuSb₂. These data were fit with a skewed Lorentzian:

$$\frac{I_E}{I_0} = W \frac{\Gamma_s^2}{\pi[(E_T - \langle E_T \rangle)^2 + \Gamma_s^2]} \{1 + \text{erf} \left[\frac{\alpha(E_T - \langle E_T \rangle)}{\sqrt{2}\Gamma_s} \right]\},$$

where W is the weight coefficient at fixed $\langle E_T \rangle$ for a given E_I and erf is the error function. The excitation width is $\Gamma_s = 3.3$ eV and the skew parameter is $\alpha = 0.29$ for the U edge data and $\Gamma_s = 4.7$ eV and $\alpha = 0.30$ for the Pu edge data.

Once the lineshape parameters were determined, an average $\langle E_T \rangle$ was found for each of the three discrete states as a function of E_I . These values were then fixed for the reported results at all E_I , except for the first peak (the f^3 peak for U edge and the f^6 peak for the Pu edge data). As noted in the text, this energy shifts by 1 to 2 eV, possibly due to a broad band for this configuration. This shift is severe enough in the PuSb₂ data so as to make it impossible to fit for individual f-configurations (see SI). Also note that the width of each peak is due to the convolution of the spectrometer and the final-state lifetime. Difference cuts along E_I showed the broadening by the intermediate-state lifetime and the mono.

In addition, below threshold, the fluorescence peak was held to zero amplitude to avoid correlations with the other peaks, mostly the f^4 peak for the Pu L_3 -edge RXES data. This constraint is not required if E_T is not allowed to vary as a function of E_I , and such fits generate configuration fractions within the stated error estimates, although the fits are of poorer quality. However, the fluorescence threshold in these fixed- E_T fits is less well defined than shown in the floating- E_T fit results in Fig. 3c and 3f. An important improvement to these methods will be better defining the relationship between the fluorescence peaks and the below-threshold peaks.

As a final note, an acceptable (but much lower quality) fit can be obtained to the entire RXES spectra with the full Kramers-Heisenberg (KH) formula (23, 25) using three discrete and three fluorescence peaks, giving lower estimates of n_f (eg. $n_f = 5.2$ for δ -Pu and 5.0 for α -Pu). We attribute the low quality of these fits to the bandwidth effects in determining E_T (not accounted for in such fits) and the use of perturbation theory in deriving the KH formula.

Acknowledgements. Work at Lawrence Berkeley National Laboratory supported by the Director, Office of Science, Office of Basic Energy Sciences (OBES), of the U.S. Department of Energy (DOE) under Contract No. DE-AC02-05CH11231. Work at Los

Alamos National Laboratory (LANL) was performed under the auspices of the U.S. DOE, OBES, Division of Materials Sciences and Engineering and funded in part by the LANL Directed Research and Development program. X-ray absorption and RXES data were collected at the Stanford Synchrotron Radiation Lightsource, a national user facility operated by Stanford University on behalf of the DOE, Office of Basic Energy Sciences. The authors acknowledge enlightening conversations with J. A. Bradley, G. Kotliar, G. H. Lander, J.-P. Rueff, J. Seidler, J. D. Thompson, and Z. Fisk.

References

1. Arko AJ, Joyce JJ, & Havela L (2006) 5f-electron phenomena in the metallic state. *The Chemistry of the Actinide and Transactinide Elements*, eds Morss LR, Edelstein NM, & Fuger J (Springer, The Netherlands), Vol 4, p 2307.
2. Stewart GR (1984) Heavy-fermion systems. *Rev. Mod. Phys.* 56:755.
3. Smith JL & Fisk Z (1982) Magnetism in Transuranics. *J. Appl. Phys.* 53(11):7883-7886.
4. Moore KT & van der Laan G (2009) Nature of the 5f states in actinide metals. *Rev. Mod. Phys.* 81(1):235.
5. Tobin JG, *et al.* (2008) On the electronic configuration in Pu: spectroscopy and theory. *J. Phys.: Condens. Matter* 20(12):125204.
6. Efremov DV, Hasselmann N, Runge E, Fulde P, & Zwicknagl G (2004) Dual nature of 5f electrons: Effect of intra-atomic correlations on hopping anisotropies. *Phys. Rev. B* 69(11):115114.
7. Park T, Graf MJ, Boulaevskii L, Sarrao JL, & Thompson JD (2008) Electronic duality in strongly correlated matter. *Proc. Natl. Acad. Sci. U. S. A.* 105(19):6825-6828.
8. Sato NK, *et al.* (2001) Strong coupling between local moments and superconducting 'heavy' electrons in UPd₂Al₃. *Nature* 410(6826):340.
9. Zwicknagl G & Fulde P (2003) The dual nature of 5f electrons and the origin of heavy fermions in U compounds. *J. Phys. Condens. Matt.* 15(28):S1911.
10. Joyce JJ, *et al.* (2006) Dual nature of the 5f electrons in plutonium materials. *Physica B* 378-80:920.
11. Lander GH, Brooks MSS, & Johansson B (1991) Orbital band magnetism in actinide intermetallics. *Phys. Rev. B* 43(16):13672-13675.
12. Lashley JC, Lawson AC, McQueeney RJ, & Lander GH (2005) Absence of magnetic moments in plutonium. *Phys. Rev. B* 72:054416.
13. Shim JH, Haule K, & Kotliar G (2007) Fluctuating valence in a correlated solid and the anomalous properties of δ -plutonium. *Nature* 446(7135):513.
14. Dallera C, *et al.* (2003) Determination of pressure-induced valence changes in YbAl₂ by resonant inelastic X-ray emission. *Phys. Rev. B* 68:245114.
15. Dallera C, *et al.* (2002) New spectroscopy solves an old puzzle: The Kondo scale in heavy fermions. *Phys. Rev. Lett.* 88:196403.
16. Bauer ED, *et al.* (2004) Investigation of Anderson lattice behavior in Yb_{1-x}Lu_xAl₃. *Phys. Rev. B* 69:125102.
17. Malterre D (1991) L_{III}-edge spectroscopy on cerium-based intermediate-valent compounds. *Phys. Rev. B* 43(2):1391.

18. Bickers NE, Cox DL, & Wilkins JW (1987) Self-consistent large-N expansion for normal-state properties of dilute magnetic alloys. *Phys. Rev. B* 36:2036.
19. Lawrence JM, Wang CH, Christianson AD, & Bauer ED (2011) Heavy fermion scaling: uranium versus cerium and ytterbium compounds. *J. Phys.-Condes. Matter* 23(9):094210.
20. Conradson SD, *et al.* (2004) Higher order speciation effects on plutonium L-3 X-ray absorption near edge spectra. *Inorg. Chem.* 43(1):116.
21. Bull MJ, McEwen KA, Osborn R, & Eccleston RS (1996) Neutron intermultiplet spectroscopy of UPd₃ and UPt₃. *Physica B* 223&224(1-4):175-177.
22. Shirley EL, Soininen JA, & Rehr JJ (2005) Modeling core-hole screening in core-excitation spectroscopies. *Phys. Scr.* T115:31-34.
23. Kotani A (2005) Resonant inelastic X-ray scattering in d and f electron systems. *Eur. Phys. J. B* 47:3-27.
24. Heathman S, *et al.* (2010) Resonant X-ray emission spectroscopy at the L₃ edge of americium up to 23 GPa. *Phys. Rev. B* 82:201103(R).
25. Glatzel P & Bergmann U (2005) High resolution 1s core hole X-ray spectroscopy in 3d transition metal complexes - electronic and structural information. *Coord. Chem. Rev.* 249:65-95.
26. Rueff J-P & Shukla A (2010) Inelastic x-ray scattering by electronic excitations under high pressure. *Rev. Mod. Phys.* 82:847-896.
27. Keski-Rahkonen O & Krause MO (1974) Total and partial atomic-level widths. *Atomic Data and Nuclear Data Tables* 14(2):139.
28. Canfield PC & Fisk Z (1992) Growth of single-crystals from metallic fluxes. *Phil. Mag. B* 65:1117.
29. Haskel D (<http://www.aps.anl.gov/xfd/people/haskel/fluo.html>).
30. McMaster W, Grande ND, Mallet J, & Hubbel J (1969) Compilation of x-ray cross sections. (Lawrence Livermore National Laboratory).
31. Lashley JC, *et al.* (2001) Low-temperature specific heat and critical magnetic field of α -uranium single crystals. *Phys. Rev. B* 63(22):224510.
32. Cornelius AL, *et al.* (1999) Electronic properties of UX₃ (X = Ga, Al, and Sn) compounds in high magnetic fields: Transport, specific heat, magnetization, and quantum oscillations. *Phys. Rev. B* 59(22):14473-14483.
33. Jiang Y, *et al.* (2011) Magnetic frustration effects in uranium intermetallics. *J. Phys., Conf. Ser.* 273:012036.
34. Mayr F, von Blanckenhagen GF, & Stewart GR (1997) Non-Fermi-liquid behavior and spin fluctuations in doped UAl₂. *Phys. Rev. B* 55(2):947-953.
35. Wang CH, *et al.* (2010) Neutron scattering and scaling behavior in URu₂Zn₂₀ and YbFe₂Zn₂₀. *Phys. Rev. B* 82(18):184407.
36. Bauer ED, *et al.* (2008) Simplifying strong electronic correlations in uranium: localized uranium heavy-fermion UM₂Zn₂₀ (M=Co,Rh) compounds. *Phys. Rev. B* 78(11):115120.
37. Tateiwa N, Sato N, & Komatsubara T (1998) Heat-capacity investigation on magnetism in UNi₂Al₃. *Phys. Rev. B* 58(17):11131 - 11133.
38. Palstra TTM, *et al.* (1985) Superconducting and Magnetic Transitions in the Heavy-Fermion System URu₂Si₂. *Phys. Rev. Lett.* 55(24):2727-2730.

39. von Blanckenhagen GF, Scheidt EW, Schreiner T, & Stewart GR (2001) Magnetism, spin fluctuations, and non-Fermi-liquid behavior in $(U_xLa_{1-x})_2Zn_{17}$. *Phys. Rev. B* 64(6):064413.
40. Sakon T, Imamura K, Koga N, Sato N, & Komatsubara T (1994) Specific heat of the heavy fermion superconductor UPd_2Al_3 . *Physica B* 199-200:154-156.
41. Tokiwa Y, *et al.* (2001) Quadrupolar phase diagram and Fermi surface properties in the localized $5f^2$ -electron system UPd_3 . *J. Phys. Soc. Japan* 70(6):1731-1743.
42. Cornelius AL, Arko AJ, Sarrao JL, & Harrison N (1999) de Haas–van Alphen effect, magnetic transitions, and specific heat in the heavy-fermion system UCd_{11} . *Phys. Rev. B* 59(21):13542-13545.
43. Lashley JC, *et al.* (2003) Experimental electronic heat capacities of α - and δ -plutonium: heavy-fermion physics in an element. *Phys. Rev. Lett.* 91:205901.
44. Javorsky P, *et al.* (2007) Specific heat and anisotropy of the nonconventional superconductors $PuCoGa_5$ and $PuRhGa_5$. *Phys. Rev. B* 75(18):184501.
45. Stewart GR & Elliott RO (1985) Anomalous behavior of $PuAl_2$. *Phys. Rev. B* 31(7):4669-4671.
46. Boulet P, *et al.* (2005) Magnetic properties of the two allotropic phases of $PuGa_3$. *Phys. Rev. B* 72:064438.
47. Sarrao JL, *et al.* (2002) Plutonium-based superconductivity above 18 K. *Nature* 420:297.
48. Bauer ED, *et al.* (2004) Structural tuning of unconventional superconductivity in $PuMGa_5$ (M=Co, Rh). *Phys. Rev. Lett.* 93:147005.

Figure legends

Fig. 1. Actinide L_3 -edge follows strongly correlated electron behavior. (a) Energy level diagram demonstrating the *dominant* transitions and the final state splitting due to the generation of the core hole, as well as the final states relationship to E_I and E_T for the RXES data. Note that other decay channels between the intermediate and final state configurations also occur (for instance, from a f^4 intermediate state to an f^5 final state); we have chosen to only illustrate the dominant channels for clarity. The intermediate states in the middle of the diagram represent the final state for the XANES data shown in (b). (b) Representative results from Pu L_3 edge XANES spectroscopy. (c,d) Linear coefficient of the low temperature specific heat in the normal state, γ , as a function of the shift of the peak in the white line relative to the α -An sample. Many of the γ values come from the literature (12, 19, 31-48). These results are available in tabular form in SI, together with individual references for the γ values.

Fig. 2. XES and RXES data on actinide intermetallics. Representative XES (a) and RXES (b) for UCd_{11} , as an example of a strongly localized An intermetallic. (c,d), Analogous data for α -Pu, as an example of a more delocalized An intermetallic. The colors in the RXES data represent the normalized emission flux. Note the clearly sharper resonance in both the XES and RXES (yellow peak) plots for the UCd_{11} compared to the α -Pu data. Similar results for $UCoGa_5$, $PuSb_2$, and δ -Pu are available in SI.

Fig. 3. Multiconfigurational orbital weights. Relative weights of the principle components to (a,b) the discrete-state excitation and the (c) fluorescence spectra for the measured U intermetallic samples. (d-f), Analogous data from the Pu intermetallics. In the case of the U intermetallics, we assign the excitations at transfer energies of 3548 eV, 3552 eV, and 3556 eV to f^3 , f^2 , and f^1 configurations based on comparisons to the oxide. Likewise for the Pu intermetallics, the excitations at 3783 eV, 3787 eV, and 3791 eV are assigned to f^6 , f^5 , and f^4 configurations. The threshold energy shift in (c) is about 2.2 eV, and in (d) is about 4.5 eV. Discrete-state peak coefficients for $PuSb_2$ are somewhat different, and are available in SI.

Table 1. *f*-orbital occupancy and configuration fraction measurements

Sample	n_f	Configuration fractions		
		f^1	f^2	f^3
UCd ₁₁	2.71	0.07	0.15	0.78
UCoGa ₅	1.92	0.32	0.44	0.24
		f^4	f^5	f^6
δ -Pu (1.9% Ga)	5.28	0.17	0.38	0.45
α -Pu	5.16	0.19	0.46	0.35

Values of the *f*-orbital occupancies, n_f , are determined by the weighted sum of the integrated intensities from each configuration peak in Fig. 3*a, b, d, and e*, for example, $n_f = (4I_4 + 5I_5 + 6I_6)/(I_4 + I_5 + I_6)$, where I_4 is the integrated intensity of the f^4 peak, etc. Absolute errors are estimated by altering the lineshape for the standard discrete excitation, and are about 10%. Relative errors between these measurements are about 2%.

Supplementary Information for “Multiconfigurational Nature of 5f Orbitals in Uranium and Plutonium Intermetallics”

C. H. Booth¹, Yu Jiang¹, D. L. Wang², J. N. Mitchell³, P. H. Tobash³, E. D. Bauer⁴, M. A. Wall⁵, P. G. Allen⁵, D. Sokaras⁶, D. Nordlund⁶, T.-C. Weng⁶, M. A. Torrez⁴, and J. L. Sarrao⁷

¹Chemical Sciences Division, Lawrence Berkeley National Laboratory, Berkeley, California 94720, USA

²Nuclear Sciences Division, Lawrence Berkeley National Laboratory, Berkeley, California 94720, USA

³Materials Science and Technology Division, Los Alamos National Laboratory, Los Alamos, New Mexico 87545, USA

⁴Materials Physics and Applications Division, Los Alamos National Laboratory, Los Alamos, New Mexico 87545, USA

⁵Condensed Matter and Materials Division, Livermore National Laboratory, Livermore, California 94550, USA

⁶Stanford Synchrotron Radiation Lightsource, SLAC National Accelerator Laboratory, Menlo Park, CA 94025, USA

⁷Science Program Office- Office of Science, Los Alamos National Laboratory, Los Alamos, New Mexico 87545, USA

Summary of file contents

These materials begin with the *Specific heat* section, which includes basic characterization details of the measured materials, focusing on the specific heat data (Fig. S1 and Table S1). The *Other Supporting Text and Figures* section shows some of the U L₃ XANES data in Fig. S2, and the available RXES and XES data from all the samples not shown in the main article (Figs. S3-S5). Finally, a RXES simulation generated from a model density of states is reported in *Example of Potential Absolute Errors and Lineshapes*, which is then fit using the skewed-Lorentzian method in the manuscript to demonstrate the method’s efficacy for discerning multiconfigurational states (Figs. S6-S7).

Specific heat and other characterization

Most of the specific heat data reported in Table S1 and Fig. 1 has been previously published. An example of data collected for this work for PuSb₂ and PuIn₃ is shown in Fig. S1, together with the measured magnetic susceptibility. The specific heat data were collected on a Quantum Design Physical Property Measurement System (PPMS) and fit using the standard form $C/T = \gamma + \beta T^2$. Since we are interested in the Kondo contributions to C/T , we do not use data when the sample is in a magnetically ordered states, as the reduction in entropy adversely affects the relationship between charge localization (Kondo temperature) and γ ¹. We therefore fit data above any magnetic transitions. The fits to data from PuSb₂ and PuIn₃ (Fig. S1) are examples of this situation. For literature data where only the low-temperature γ is reported, we refit the data as just described. Other samples where magnetic transitions occur include Pu₂Ni₃Si₅ and PuGa₃. A source of error arises if the data above, say, $T = \Theta_D/10$, where Θ_D is the Debye temperature derived from β . By fitting C/T data from samples that do not order magnetically with similar Θ_D , such as YbAgCu₄, we find that fits to near 20 K are about 10% high compared to fits to the low-temperature data. For all such fits reported here, we attached an error of 100 mJ mol⁻¹ K⁻² as a conservative estimate. Note that all data reported here are not, where possible, corrected for the lattice contribution via subtraction using a nonmagnetic analogue, since much of the literature data would not be directly comparable.

Other Supporting Text and Figures

Representative U L₃ XANES data are shown in Fig. S2. RXES and XES data for δ -Pu are shown in Fig. S3. These data are very similar to the data from α -Pu (Fig. 2). Data on UCoGa₅ are shown in Fig. S4, and data from PuSb₂ are shown in Fig. S5. These latter data have some different properties, as discussed forthwith.

The data from PuSb₂ (Fig. S5) shows a single discrete excitation at energies below the fluorescence threshold. In contrast to data from the other measured materials, the energy position of this peak does not stay roughly constant with E_I (Fig. S5d), but instead shifts from about 3778 eV to 3782 eV while the peak has significant weight in the spectrum (Fig. S5c). Over this energy range, the peak width does not change, and is, in fact, quite narrow as mentioned above, with $\Gamma_S = 4.7$ eV. The lack of change and overall sharpness of this peak does not allow for an interpretation with a significant multiconfigurational state; however, due to the large energy shift, we cannot uniquely assign the f -occupancy of this single configuration. The shift of the single-state E_T requires further study, but is likely due to a larger bandwidth in the unoccupied d -states below the fluorescence threshold than in the other measured samples.

Example of Potential Absolute Errors and Lineshapes

The procedure used for fitting the data discussed in this work involves fitting skewed Lorentzians to the features in the XES data, as discussed in the main work. The absolute

quoted estimated error of 10% was estimated by using different, generally less satisfactory lineshapes. Here we give an example of one particular method that eventually may lead to better lineshapes. In this example, we choose a single-configurational density of unoccupied electronic states (DOS) and then fit this simulated data using the methods used in the paper to fit the data.

The chosen DOS is shown in Fig. S6a, and is comprised essentially of a step function added to a Lorentzian. This DOS is then used to generate the PFY in Fig. S6b and a full RXES spectrum, as shown in Fig. S6c, by making use of the KH formula and following Eq. 19 in Rueff and Shukla's review article (21):

$$I_E \propto \sum \sum \int d\varepsilon \frac{\eta(\varepsilon)}{(E_{ig} + \varepsilon - E_I)^2 + \Gamma_i^2/4} \times \frac{\Gamma_f/2\pi}{(E_{fg} + \varepsilon - E_T)^2 + \Gamma_f^2/4},$$

where $\eta(\varepsilon)$ is the DOS and ε is the energy with respect to the Fermi level, Γ_f and Γ_i are the width of the final and intermediate states, and E_{fg} and E_{ig} are the threshold energies. Interference terms are neglected here. These values were chosen to reflect data for the U_{LIII} edge.

As in the paper, we determine the so-called fluorescence lineshape fit parameters by fitting to these simulated data well above the edge, and the discrete lineshape parameters well below the edge. The inclusion of a sharp peak in the DOS was determined to be necessary to obtain simulated data well below the edge that is not overly skewed. The skew parameter $\alpha \approx 0.23$ in this simulation, close to that found for fits to all the real data ($\alpha \approx 0.30$). It is important to note that a step-function DOS without the sharp peak gave a much larger skew parameter ($\alpha \approx 9$).

Once the lineshapes were determined, we fit the simulated XES data assuming three peaks: the fluorescence peak and two discrete peaks. The energy of the second peak is fixed at 4 eV above the main peak to avoid it floating uncontrollably in these simulation fits. Fit examples are shown in Fig. S7a and Fig. S7b. Fitting all the XES data at all EI and results in amplitudes for each peak as a function of EI shown in Fig. S7c. Indeed, adding the second discrete peak does improve the fit. However, the integrated area under the curves indicates the first discrete peak (P2) accounts for 91% of the total amplitude of P2 and P3. Since the DOS is, in fact, a single configuration, the fit results indicate that the method is consistent with a single configuration with 10%, consistent with the stated absolute error in the paper.

References

1. Lashley JC, *et al.* (2001) Low-temperature specific heat and critical magnetic field of α -uranium single crystals. *Phys. Rev. B* 63(22):224510.
2. Cornelius AL, *et al.* (1999) Electronic properties of UX_3 (X = Ga, Al, and Sn) compounds in high magnetic fields: Transport, specific heat, magnetization, and quantum oscillations. *Phys. Rev. B* 59(22):14473-14483.
3. Jiang Y, *et al.* (2011) Magnetic frustration effects in uranium intermetallics. *J. Phys., Conf. Ser.* 273:012036.
4. Mayr F, von Blanckenhagen GF, & Stewart GR (1997) Non-Fermi-liquid behavior and spin fluctuations in doped UAl_2 . *Phys. Rev. B* 55(2):947-953.
5. Wang CH, *et al.* (2010) Neutron scattering and scaling behavior in URu_2Zn_{20} and $YbFe_2Zn_{20}$. *Phys. Rev. B* 82(18):184407.
6. Bauer ED, *et al.* (2008) Simplifying strong electronic correlations in uranium: localized uranium heavy-fermion UM_2Zn_{20} (M=Co,Rh) compounds. *Phys. Rev. B* 78(11):115120.
7. Lawrence JM, Wang CH, Christianson AD, & Bauer ED (2011) Heavy fermion scaling: uranium versus cerium and ytterbium compounds. *J. Phys.-Condes. Matter* 23(9):094210.
8. Tateiwa N, Sato N, & Komatsubara T (1998) Heat-capacity investigation on magnetism in UNi_2Al_3 . *Phys. Rev. B* 58(17):11131 - 11133.
9. Palstra TTM, *et al.* (1985) Superconducting and Magnetic Transitions in the Heavy-Fermion System URu_2Si_2 . *Phys. Rev. Lett.* 55(24):2727-2730.
10. von Blanckenhagen GF, Scheidt EW, Schreiner T, & Stewart GR (2001) Magnetism, spin fluctuations, and non-Fermi-liquid behavior in $(U_xLa_{1-x})_2Zn_{17}$. *Phys. Rev. B* 64(6):064413.
11. Sakon T, Imamura K, Koga N, Sato N, & Komatsubara T (1994) Specific heat of the heavy fermion superconductor UPd_2Al_3 . *Physica B* 199-200:154-156.
12. Tokiwa Y, *et al.* (2001) Quadrupolar phase diagram and Fermi surface properties in the localized $5f^2$ -electron system UPd_3 . *J. Phys. Soc. Japan* 70(6):1731-1743.
13. Cornelius AL, Arko AJ, Sarrao JL, & Harrison N (1999) de Haas-van Alphen effect, magnetic transitions, and specific heat in the heavy-fermion system UCd_{11} . *Phys. Rev. B* 59(21):13542-13545.
14. Lashley JC, *et al.* (2003) Experimental electronic heat capacities of α - and δ -plutonium: heavy-fermion physics in an element. *Phys. Rev. Lett.* 91:205901.
15. Lashley JC, Lawson AC, McQueeney RJ, & Lander GH (2005) Absence of magnetic moments in plutonium. *Phys. Rev. B* 72:054416.
16. Javorsky P, *et al.* (2007) Specific heat and anisotropy of the nonconventional superconductors $PuCoGa_5$ and $PuRhGa_5$. *Phys. Rev. B* 75(18):184501.
17. Stewart GR & Elliott RO (1985) Anomalous behavior of $PuAl_2$. *Phys. Rev. B* 31(7):4669-4671.
18. Boulet P, *et al.* (2005) Magnetic properties of the two allotropic phases of $PuGa_3$. *Phys. Rev. B* 72:064438.
19. Sarrao JL, *et al.* (2002) Plutonium-based superconductivity above 18 K. *Nature* 420:297.

20. Bauer ED, *et al.* (2004) Structural tuning of unconventional superconductivity in PuMGa_5 (M=Co, Rh). *Phys. Rev. Lett.* 93:147005.
21. Rueff J-P & Shukla A (2010) Inelastic x-ray scattering by electronic excitations under high pressure. *Rev. Mod. Phys.* 82:847-896.

Figure legends

Figure S1 | Specific heat examples. a,b, Specific heat data from (a) PuSb₂ ($\gamma = 397 \text{ mJ mol}^{-1} \text{ K}^{-2}$) and (b) PuIn₃ ($\gamma = 326 \text{ mJ mol}^{-1} \text{ K}^{-2}$), as examples where a linear fit was extrapolated from above an antiferromagnetic transition at relatively high T.

Figure S2 | Representative U L₃ edge XANES data for several samples. All these data are collected at $T \approx 30 \text{ K}$.

Figure S3 | RIXS results for δ -Pu. a,b, RIXS data (a) and XES at several incident energies (b) for δ -Pu.

Figure S4 | RIXS results for UCoGa₅. a,b, RIXS data (a) and XES at several incident energies (b) for UCoGa₅.

Figure S5 | RXES results on PuSb₂. a, XES at several incident energies for PuSb₂. **b-d,** RXES data (b) and fit results showing the single discrete excitation (c) amplitude and (d) peak transfer energy.

Figure S6 | Single-configuration simulation. a, DOS and PFY of simulated RXES. The partial fluorescence yield (PFY) shows the diagonal cut through the RXES simulated data in (b). **b,** RXES simulation. **c,** XES cuts at fixed E_I .

Figure S7 | XES and fit results for single-configuration simulation. a, XES and fit results for $E_I=17160 \text{ eV}$ to simulation in Fig. S6. P1 indicates the fluorescence peak, and P2 and P3 are discrete excitations 4 eV apart. Fit results to this simulation follow the methods outlined in the main paper. **b,** XES and fit results for $E_I=17170 \text{ eV}$ of simulation in Fig. S6. **c,** Amplitudes for each fitted peak as a function of E_I . Integrated amplitudes indicate P2 makes up 91% of the amplitude of P2+P3.

Table S1. Data used to generate Fig. 1, together with the literature source for the specific heat results. All values of γ are obtained above any noted transitions. The ground state of each sample is also noted: sc=superconductor, pm=paramagnet, afm=antiferromagnet, sf=spin fluctuation, sg=spin glass, and qo=quadrupolar order. Specific heat data are per mol An. L_3 peak position errors are less than 0.1 eV, and are calibrated to the first inflection point of the dioxide at 17166.0 eV for UO_2 and 18062.3 eV for PuO_2 .

<i>compound</i>	<i>ground state</i>	L_3 peak position (eV)	γ ($\text{mJ} \cdot \text{mol}^{-1} \cdot \text{K}^{-2}$)	γ source
α -U	sc (0.5 K)	17173.1	9.13	(1)
UCoGa_5	pm	17172.8	21	this work
USn_3	pm	17172.5	172	(2)
UAuCu_4	afm (30 K)	17171.9	100	(3)
UAl_2	sf	17171.9	70 ^a	(4)
$\text{URu}_2\text{Zn}_{20}$	pm	17171.7	190	(5)
UAu_3Ni_2	sg (3.6 K)	17171.6	270	(3)
$\text{UCo}_2\text{Zn}_{20}$	pm	17171.6	151 ^e	this work ^c
$\text{UFe}_2\text{Zn}_{20}$	pm	17171.5	176	(6)
UCu_5	afm (15 K)	17171.5	203	this work
UPt_3	sf	17171.4	225	(7)
UNi_2Al_3	afm (4.6 K)	17171.4	129	(8)
UAuPt_4	sf	17171.1	260	(3)
URu_2Si_2	afm (17.5 K)	17171.0	180	(9)
U_2Zn_{17}	afm (9.7 K)	17170.4	412	(10)
UPd_2Al_3	afm (14 K), sc (2 K)	17170.4	210	(11)
UPd_3	qo (7.5 K)	17170.4	280 ^d	(12)
UCd_{11}	afm (5 K)	17166.5	840	(13)
UO_2	afm (30.8 K)	17172.2	-	
α -Pu	pm	18068.2	17	(14)
δ -Pu (1.9 at% Ga)	pm	18066.9	42	(15)
PuCoGa_5	sc (18.2 K)	18066.1	130 ^b	(16)
Pu_2PtGa_8	pm	18065.3	51	this work
PuAl_2	afm (3.5 K)	18065.2	260	(17)
PuCoIn_5	sc (2.7 K)	18064.7	231	this work
PuPt_2In_7	pm	18064.4	250	this work
PuGa_3	afm (24 K)	18064.4	412 ^{c,d}	(18)
$\text{Pu}_2\text{Ni}_3\text{Si}_5$	afm (35 K)	18064.3	476 ^c	this work
PuIn_3	afm (14.6 K)	18064.2	325	this work
PuSb_2	afm (20 K)	18063.5	397 ^c	this work
PuO_2	pm	18068.4	-	

^a γ determined at high magnetic field to reduce spin fluctuations.

^b An alternate value is 77 $\text{mJ} \cdot \text{mol}^{-1} \cdot \text{K}^{-2}$ (19). The change at T_c gives 95 $\text{mJ} \cdot \text{mol}^{-1} \cdot \text{K}^{-2}$ (20)

^c These values for γ are extrapolated from data above 20 K due to relatively high Néel temperatures, and so are less reliable. These data are marked with 100 $\text{mJ} \cdot \text{mol}^{-1} \cdot \text{K}^{-2}$ error bars in Fig. 1.

^d These values for γ are obtained by refitting the data in the cited reference above the listed phase transition.

^e Fits to C/T data by Wang et al. (5) give $\gamma = 558 \text{ mJ} \cdot \text{mol}^{-1} \cdot \text{K}^{-2}$ at $T=0$ K, but this result does not hold for higher T . The presence of antiferromagnetic fluctuations likely enhances γ . The value reported here is for a higher temperature fit between 10-15 K on data from a new sample.

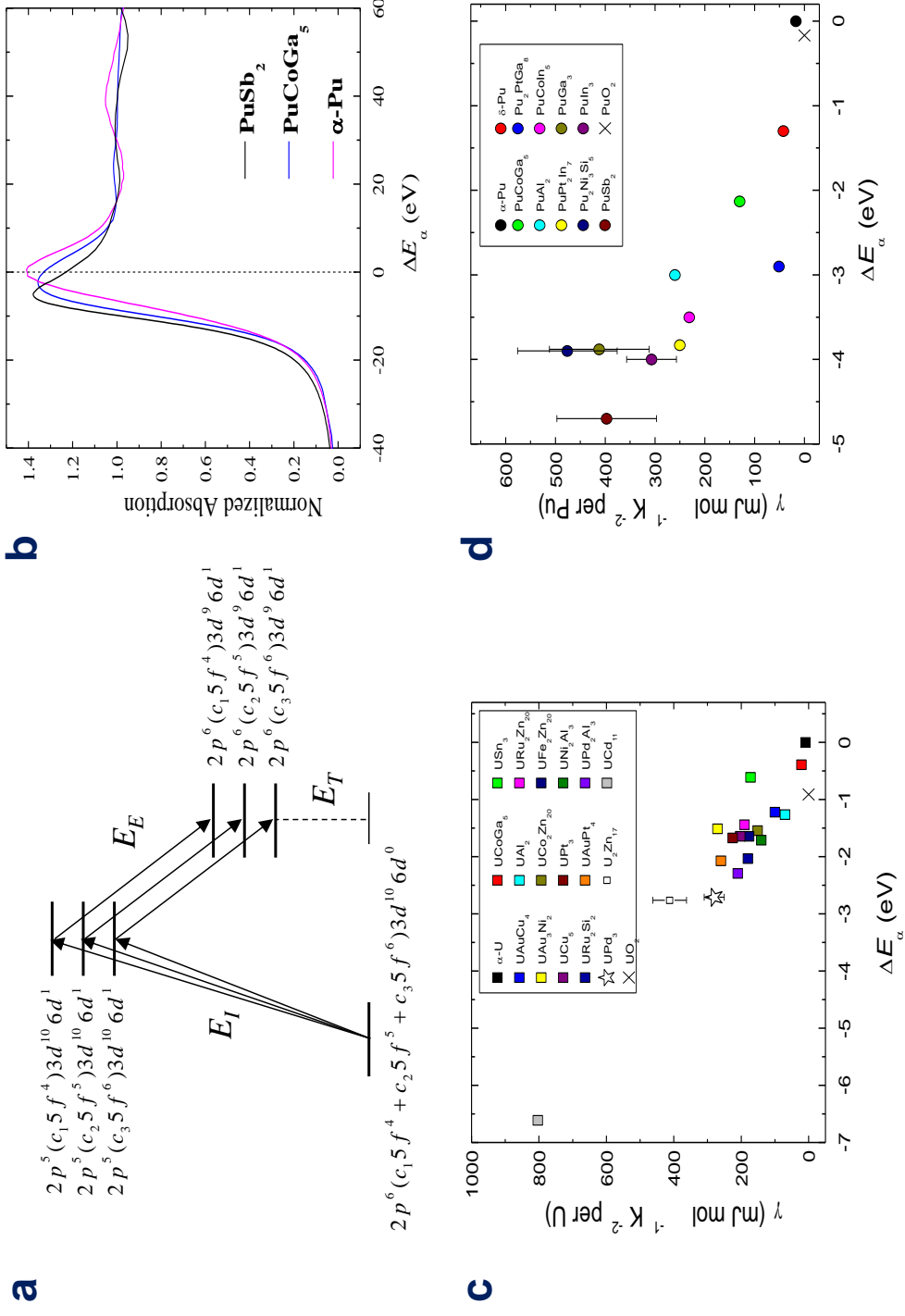


Figure 1

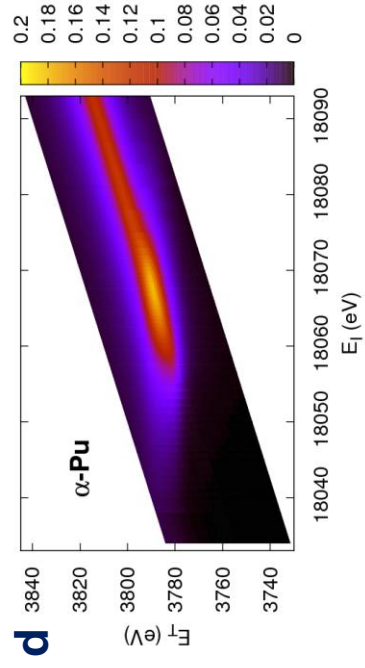
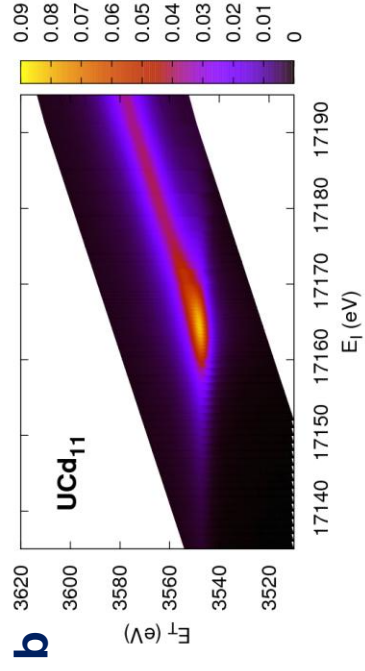
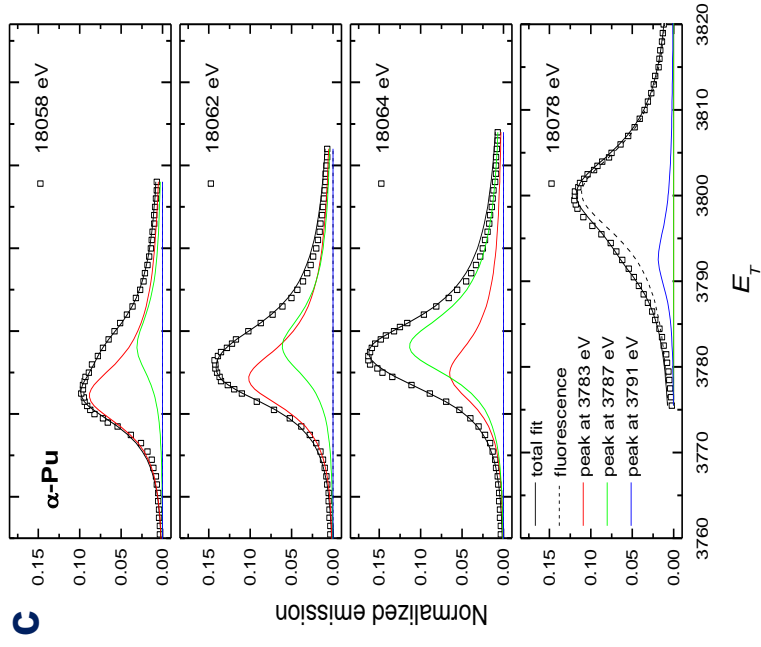
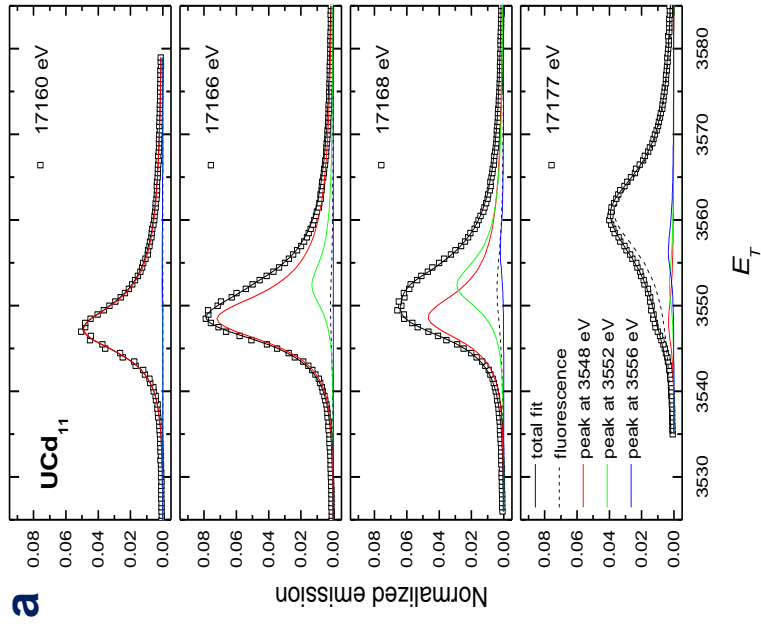


Figure 2

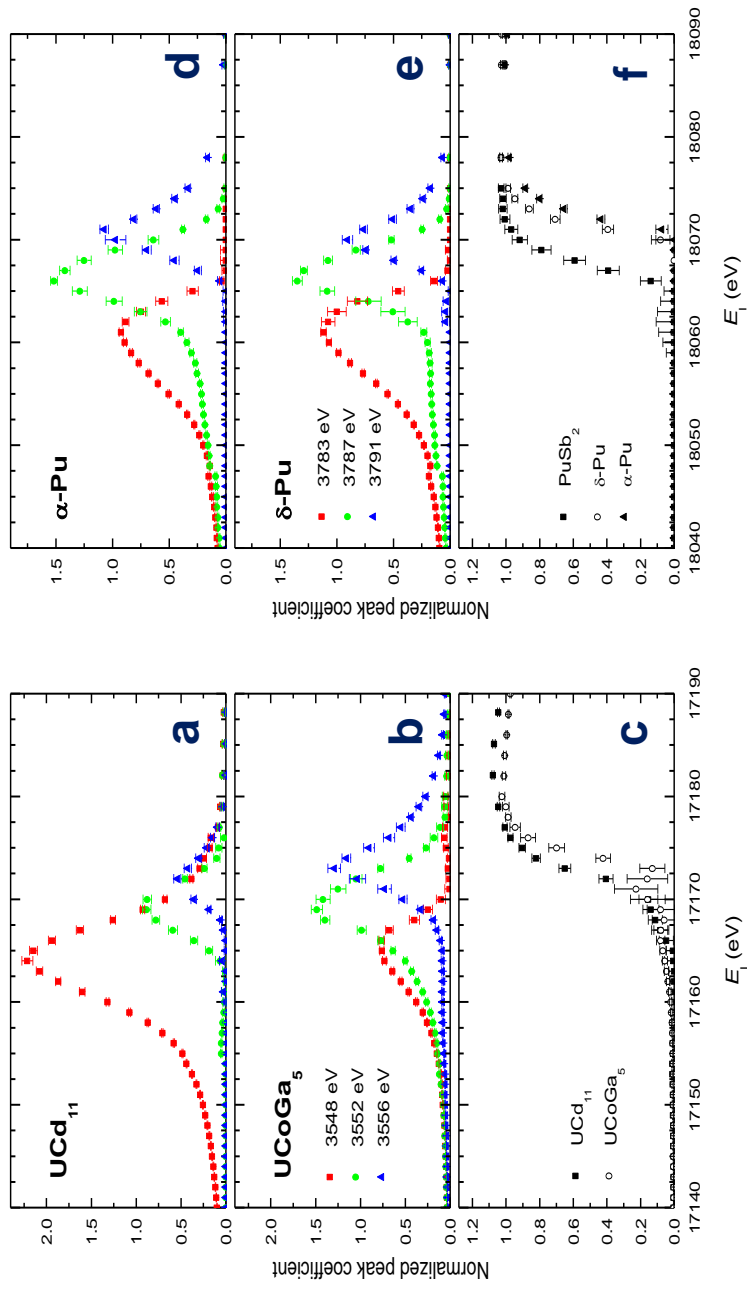


Figure 3

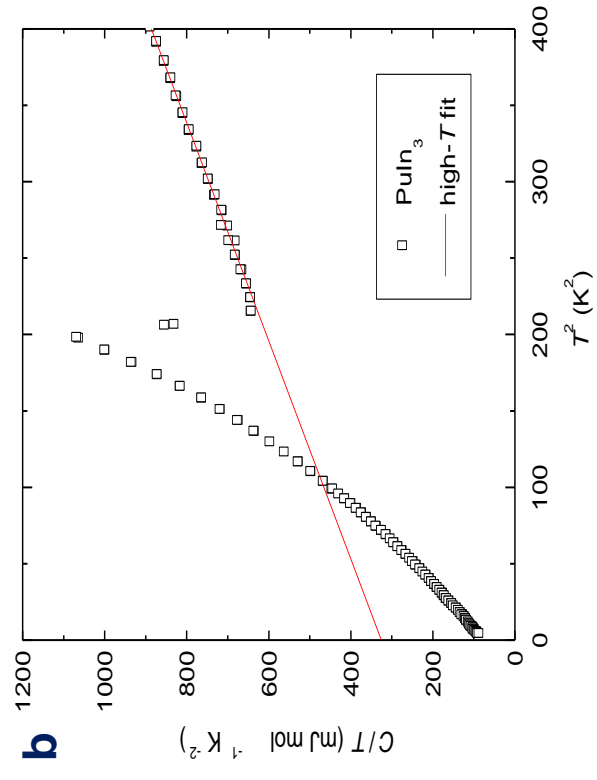
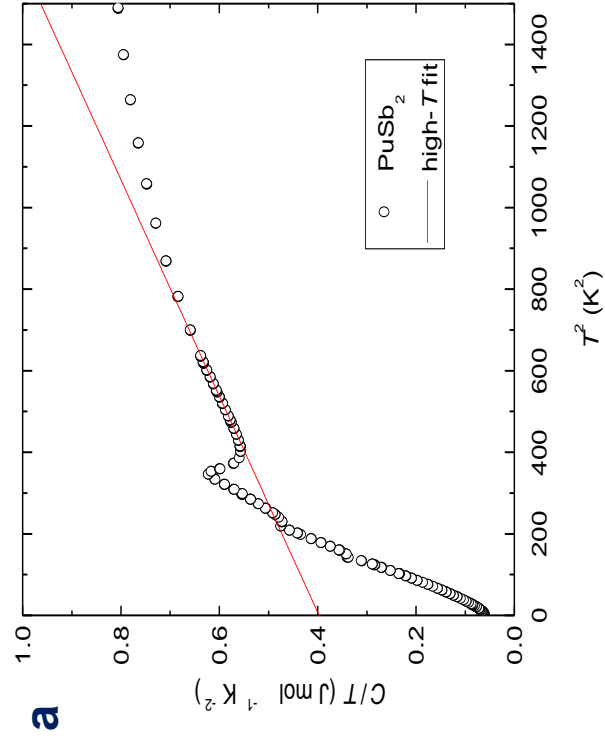


Figure S1

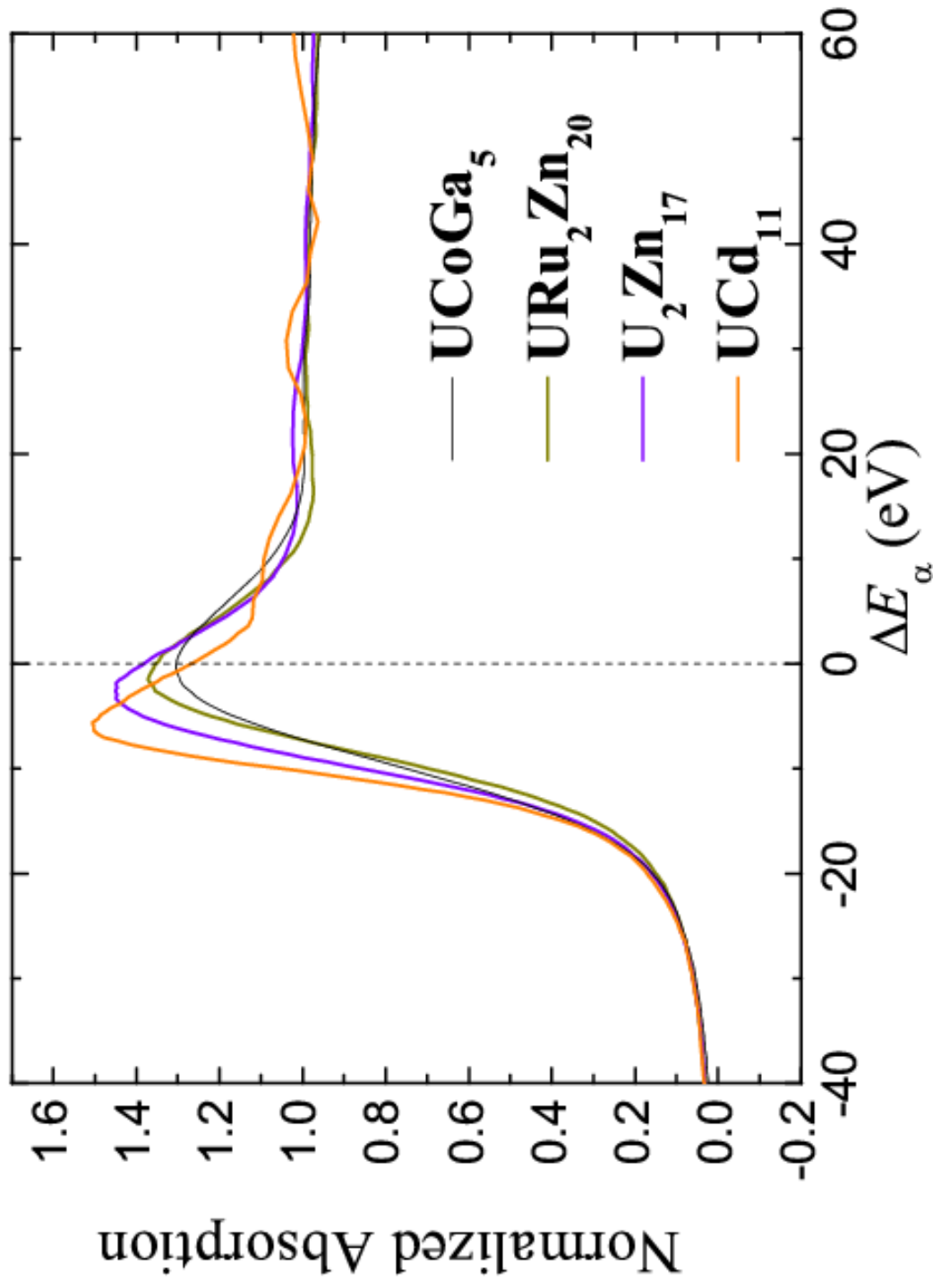


Figure S2

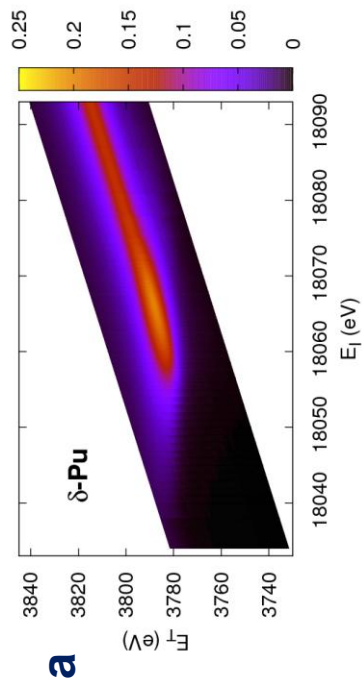
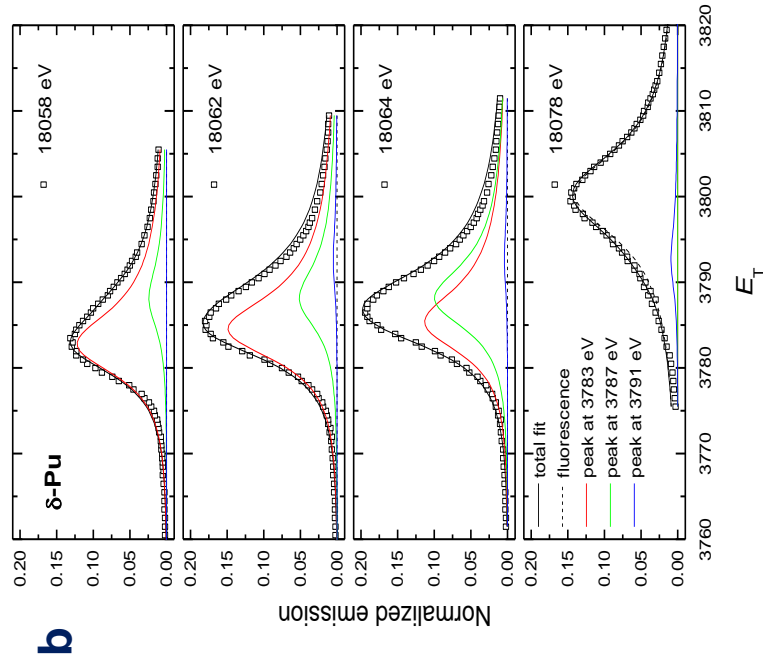


Figure S3

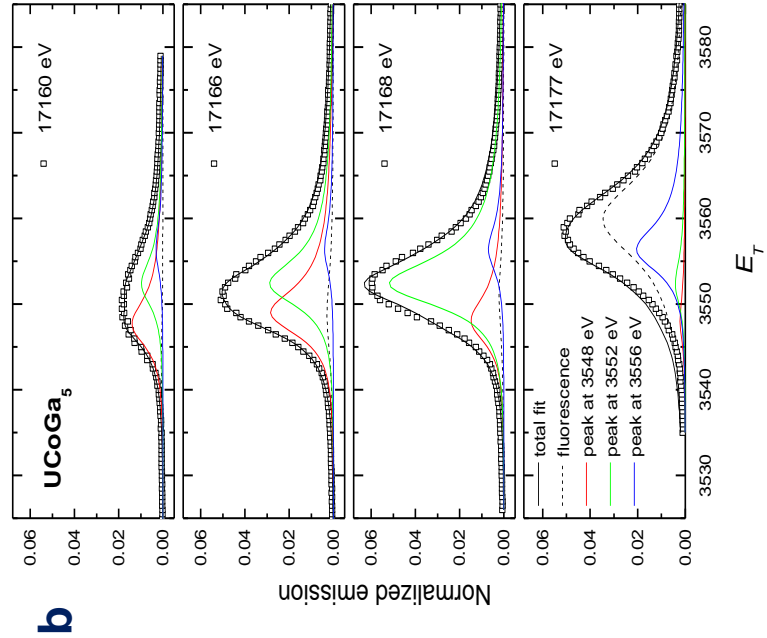


Figure S4

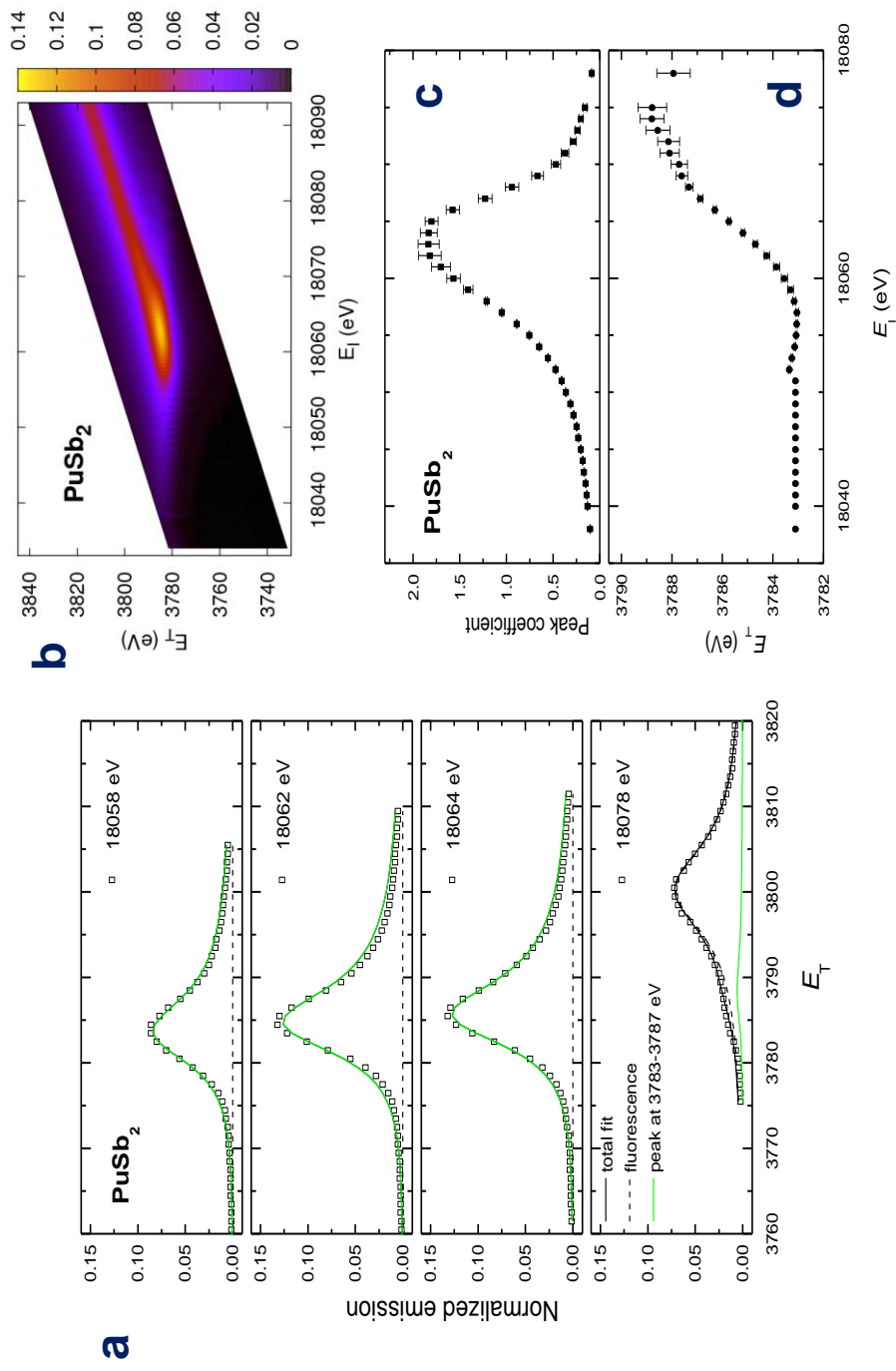


Figure S5

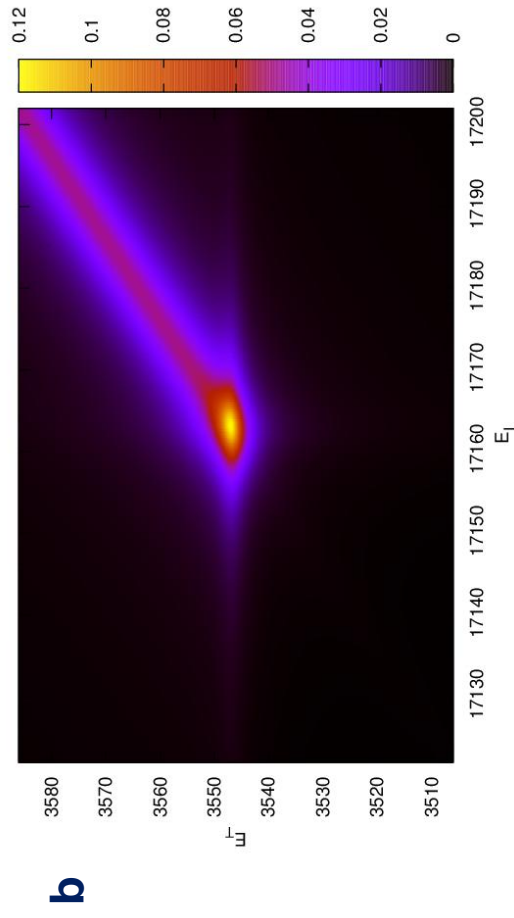
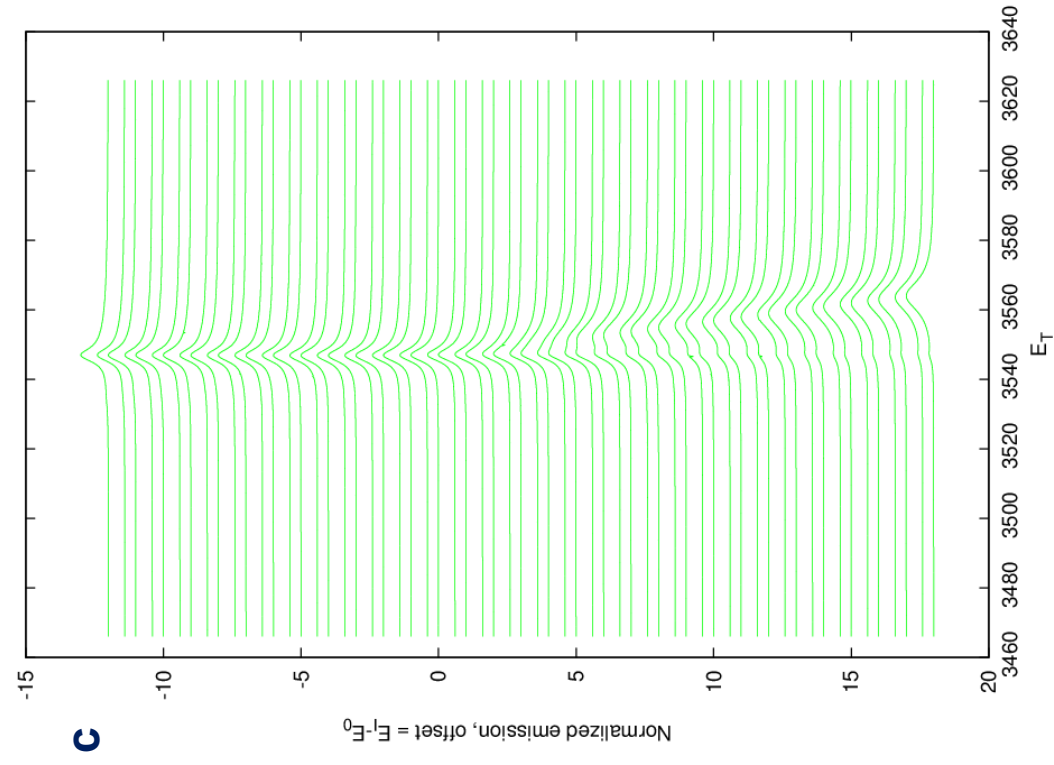
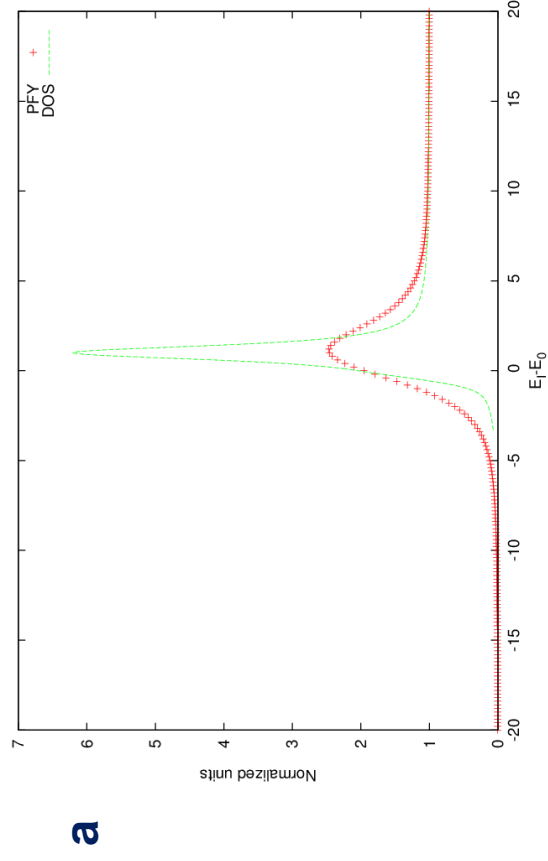


Figure S6

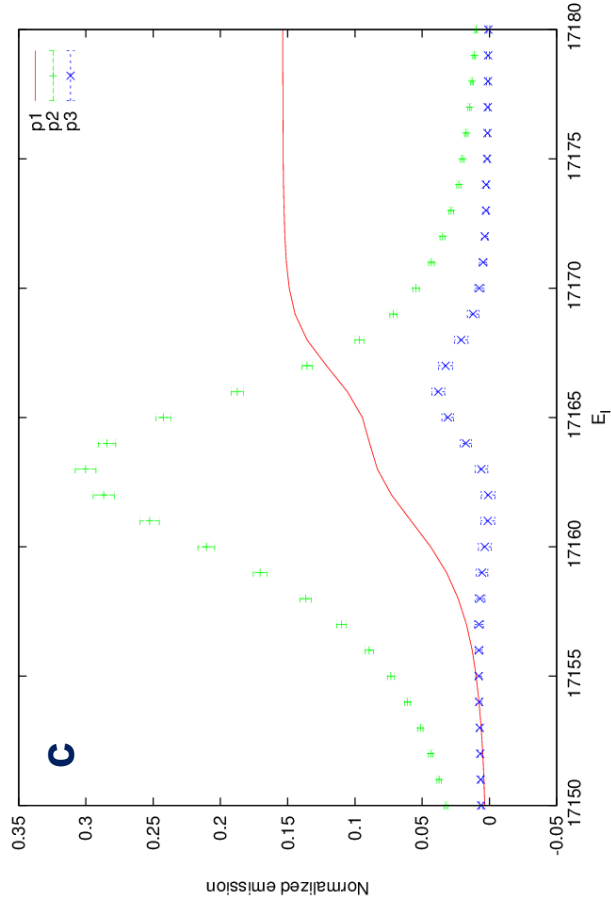
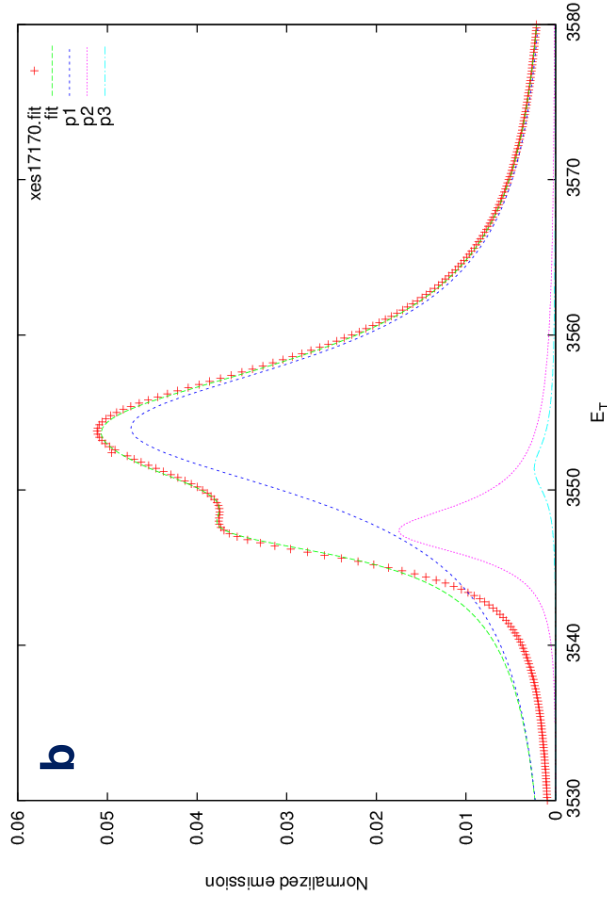
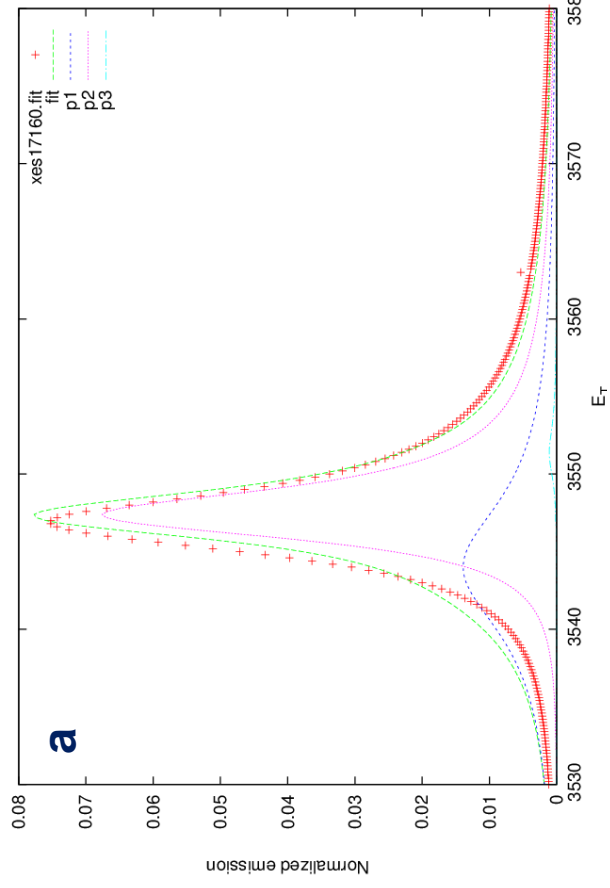


Figure S7

DISCLAIMER

This document was prepared as an account of work sponsored by the United States Government. While this document is believed to contain correct information, neither the United States Government nor any agency thereof, nor the Regents of the University of California, nor any of their employees, makes any warranty, express or implied, or assumes any legal responsibility for the accuracy, completeness, or usefulness of any information, apparatus, product, or process disclosed, or represents that its use would not infringe privately owned rights. Reference herein to any specific commercial product, process, or service by its trade name, trademark, manufacturer, or otherwise, does not necessarily constitute or imply its endorsement, recommendation, or favoring by the United States Government or any agency thereof, or the Regents of the University of California. The views and opinions of authors expressed herein do not necessarily state or reflect those of the United States Government or any agency thereof or the Regents of the University of California.